Study of Electrical and Optical Peaking of Si Ring Modulators for Tailoring Modulation Band

Hsiang-Chih Kao, Ming-Wei Lin, and Ming-Chang M. Lee

***Abstract*—An operation scheme using electrical peaking and optical peaking to engineer the modulation band of a Si microring modulator is presented. By incorporating an inductor design at the metal traces of a Si microring modulator, the driving signal can be magnified near the peaking frequency. Although adjusting the wavelength detuning of a ring modulator also introduces optical peaking to extend the 3-dB roll-off frequency, using inductive peaking has no detrimental effect on the low-frequency response. By exploiting both effects, the modulation band can be tailored with more degrees of freedom. We accomplish a Si microring modulator design with a wide and flat transmission band over 95 GHz, which is potentially applied for a non-return-to-zero (NRZ) data transmission over 120 Gbit/s without extra signal post-compensation.**

***Index Terms*—Silicon photonics, optical transmitters, optical communication, optical modulators, electro-optical modulators, and optical ring resonators.**

I. Introduction

With the booming growth of information technologies nowadays such as 5th-generation (5G) wireless system, virtual and augmented reality (AR/VR), artificial intelligence (AI), unmanned vehicle (UV) and internet of things (IoT), high-speed, high-density, and real-time data transmission becomes essential among hardware to exchange the information. Optical communication is no doubt the backbone technology to fulfill the requirement of data transmission in all aspects. In recent years, silicon photonics [1], [2] receives a lot of attention and has been considered an ideal platform to implement a large-scale optical system on a chip, due to the unique advantages of a well-developed fabrication ecosystem shared with the IC industry and the capability of mass production.

One of the key components in Si photonics is high-speed modulators. Three types of high-speed modulators are mainly employed, which are the Si Mach-Zehnder modulator (MZM) [3], [4], Si microring modulator (MRM) [5], [6], [7], [8] and SiGe electro-absorption modulator (EAM) [9], [10]. Si MZM can operate with a high modulation depth and is less sensitive to temperature variation, but it usually requires a large device footprint and has high power consumption. SiGe EAM can perform at a very high speed; however, the operating wavelength window is limited, and it is difficult to monolithically integrate with Ge photodetectors. On the other hand, Si MRM is advantageous in device compactness and low power consumption, although a feedback control circuit is usually required to stabilize the resonant wavelength.

Recently, several reports showed the electrical-to-optical (EO) conversion efficiency of Si modulators can be enhanced by engineering the position and shape of the depletion region, such as an L-shape or U-shape doping around the waveguide core [11], [12]. In addition, the EO conversion bandwidth of a Si MRM can be tuned by the optical peaking effect [13], [14], [15], [16], which is correlated with the dynamics of modulated-wave actions in an optical cavity depending on the wavelength detuning (difference between the resonant wavelength and the operating wavelength). By exploiting the optical peaking effect, the 3dB roll-off frequency of the Si MRM can be extended. Nevertheless, the low-frequency response of EO conversion is suppressed, which could cause ripples in the time domain. The eye diagram of demodulated signals would look asymmetric, and the nonlinear response becomes prominent [17]. Signal post-processing and pre-emphasis are required to compensate such a distortion, resulting in complexity in the transmitter or receiver circuit design. On the other hand, it is also known that inductive peaking can be applied to improve the bandwidth of ring modulators [26].

Previously, we have demonstrated a Si MRM with an operating bandwidth over 65 GHz via the inductive peaking scheme [27]. In this paper, we comprehensively study the EO conversion response of a Si MRM based on the transfer function of an equivalent circuit model according to the MRM structure and operating condition. By adding an inductor in the metal traces of the Si MRM, an inductive peaking technique can be simply applied to modify the electrical response of input signals delivered to the microring component. Meanwhile, by adjusting the wavelength detuning, optical peaking is employed to further alter the EO response. Both the inductive peaking and optical peaking effects can be utilized to tailor the modulation band of the Si MRM. We find that the Si MRM can be designed with a multiplied gain at a specific modulation frequency by engineering the inductive and optical peaking frequencies near it, or we can accomplish a broad and flat modulation band

Manuscript received 9 April 2023; revised 7 May 2023; accepted 18 May 2023. Date of publication 22 May 2023; date of current version 29 May 2023. This work was supported by the National Science and Technology Council of Taiwan under Grants NSTC-110-2224-E-007-005 and NSTC-112-2119-M-007-006. *(Corresponding author: Ming-Chang M. Lee.)*

Hsiang-Chih Kao was with the Institute of Photonics Technologies, National Tsing Hua University (NTHU), Hsinchu 300, Taiwan, and also with the Taiwan Semiconductor Research Institute (TSRI), Hsinchu 300, Taiwan. He is now with the Realtek, Hsinchu 300, Taiwan (e-mail: rich.kao@realtek.com).

Ming-Wei Lin is with the Taiwan Semiconductor Research Institute (TSRI), Hsinchu 300, Taiwan (e-mail: mwlin@narlabs.org.tw).

Ming-Chang M. Lee is with the Institute of Photonics Technologies and the Department of Electrical Engineering faculty, National Tsing Hua University (NTHU), Hsinchu 300, Taiwan (e-mail: mclee@ee.nthu.edu.tw).

Digital Object Identifier 10.1109/JPHOT.2023.3278856

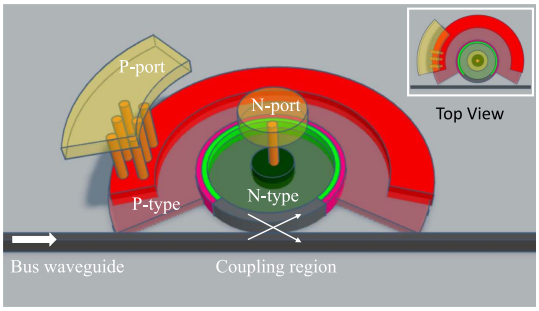

Fig. 1. Schematic illustration of a depletion-type Si microring modulator. The green and red colors represent the p- and n-type Si respectively.

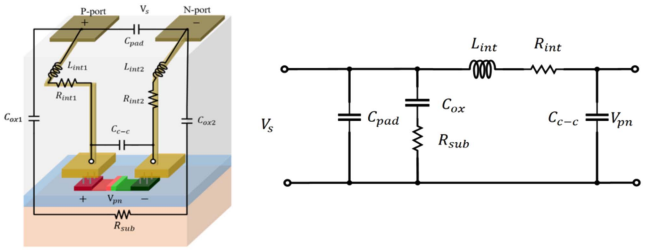

Fig. 2. Equivalent circuit model of the metal traces and pads connecting to the Si MRM: (a) The parasitic electrical elements and (b) the circuitry presentation.

by properly choosing the optical detuning condition for the maximal low-frequency EO response and extending the 3-dB roll-off frequency via inductive peaking. The former scheme can be applied for 5G FR2 mmWave photonics and the latter can be utilized for high-speed data transmission.

II. Device Configuration and the Circuit Model of Driving a Si MRM

Fig. 1 shows the device configuration of a depletion-type Si MRM studied in this paper. The Si microring is made of a Si rib waveguide with a height of 220 nm and a width of 500 nm, coupled to a 450 nm wide bus waveguide. The slab thickness of the rib waveguide is 70 nm. The microring radius is 5 μm, and the gap between the ring and the bus waveguide is about 160 nm. To modulate the free carrier density inside the ring, a p-n junction is positioned near the middle of the ring waveguide. Around 75% of the microring is covered with the p-n junction.

To drive the Si MRM, external signals are applied on the signal and ground pads and then transmitted to the device through metal lines and vias. These electrical paths will introduce an additional parasitic effect, as shown in Fig. 2. When the modulation speed increases, the parasitic elements can't be ignored. Meanwhile, the signal transferred to the p-n junction of the Si MRM can also be described by a circuit model illustrated in Fig. 3. All these circuit elements [18] depend on the structural dimension, spacing, and material resistivity and permittivity. Note that the dopant concentration and position of the Si p-n junction also affect the modulation efficiency, speed, and optical insertion loss of an MRM [19]. However, it is beyond the scope of this study. We estimate the wavelength shift of the MRM is about 25 pm/V under a reverse bias of 2V.

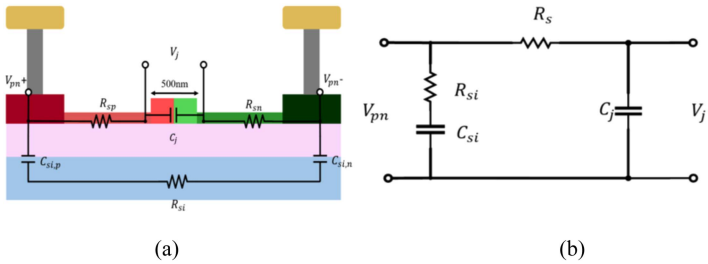

Fig. 3. Equivalent circuit model of the p-n junction in the Si MRM: (a) The parasitic electrical elements and (b) the circuitry presentation.

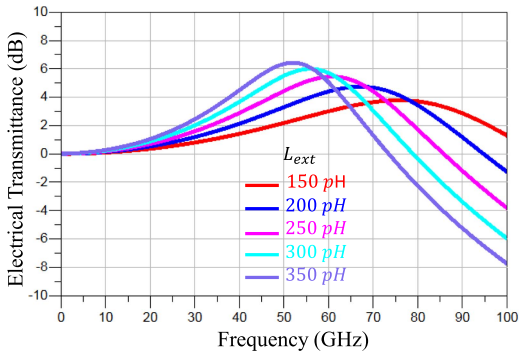

Fig. 4. Inductive peaking effect of the driving voltage on the Si MRM with respect to different extrinsic inductances.

We first analyze the equivalent circuit of parasitic elements on a Si MRM (Fig. 2), which is contributed by those elements at the pads, metal traces, and vias. C_{pad} is the capacitance between two pads, and C_{ox} is the total capacitance between the pads and the silicon substrate ($C_{ox} = C_{ox1} \| C_{ox2}$). V_s is the applied signal from the driver. R_{sub} represents the resistance of the AC current passing through C_{ox} and the silicon substrate. R_{int} and L_{int} are the total resistance and inductance attributed to the metal structures including the metal lines, pads and vias, respectively ($R_{int} = R_{int1} + R_{int2}$, $L_{int} = L_{int1} + L_{int2}$). C_{cc} is the capacitance between vias. Next, we examine the equivalent circuit model of the p-n junction in the microring waveguide (Fig. 3). C_j is the junction capacitance and R_s represent the total resistance in the p- and n-doped regions. C_{si} is the parasitic capacitance between the doped SOI and the silicon substrate and R_{si} represents the parasitic resistance of the silicon substrate below the p-n junction. All these component parameters can be obtained through a device simulation by TCAD (Synopsys), according to the lumped model of the device structure. The ultimate voltage (V_j) across the depletion region is analyzed by cascading these two circuit models together.

To accomplish the inductive peaking scheme, we re-design the metal traces to introduce an extra inductance in the first-stage equivalent circuit (Fig. 2). The inductor could be a planar coil or a specifically designed metal segment. Therefore, the intrinsic parasitic inductance and resistance, L_{int} and R_{int}, are modified to the extrinsic inductance and resistance L_{ext} and R_{ext}, depending on the designed metal structures to achieve the desired transmission spectrum. Fig. 4 shows the frequency response of V_j with respect to different extrinsic inductances, from 150 to 350 pH

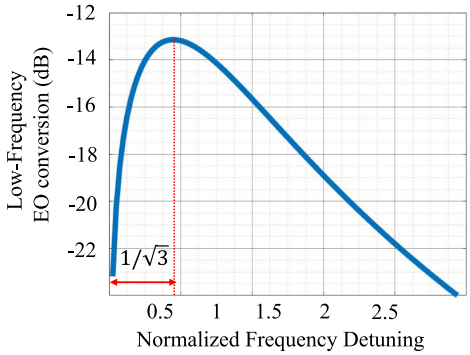

Fig. 5. Low-frequency EO conversion efficiency of the Si MRM as a function of optical frequency detuning. The Si MRM is assumed to operate near the critical coupling condition. The driving voltage is 1 V.

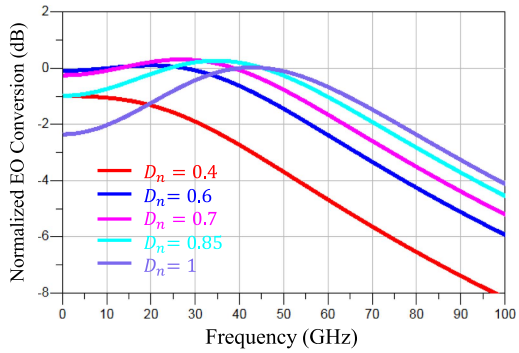

Fig. 6. Frequency response of EO conversion for the Si MRM with respect to different normalized optical frequency detuning.

with an increment of 50 pH. In general, the peaking frequency decreases with the inductance while the peaking gain increases.

III. Electrical-to-Optical Conversion of a Silicon Microring Modulator

Next, we investigate the dynamics of wavelength-dependent EO conversion of the Si MRM. Here we assume the effective-index variation of the Si waveguide is a linear function of a small signal applied on the p-n junction. According to the coupled-mode theory [13] of a microcavity, the transfer function of EO conversion for the Si MRM in the s-domain can be expressed by [20], [21], [22].

$$\frac{P_{out}}{V_j P_{in}} = \mathrm{EO}\,(\mathrm{s}) = \frac{4}{n_g}\cdot\frac{\partial n}{\partial V_j}\cdot\frac{\omega_0\frac{D}{\tau_e}}{D^2+\frac{1}{\tau^2}}\cdot\frac{s+\frac{1}{\tau}}{s^2+\frac{2}{\tau}s+D^2+\frac{1}{\tau^2}} \quad (1)$$

$$D = |\omega-\omega_0| \quad (2)$$

where V_j is the phasor of a small signal across the p-n junction, P_{out}/P_{in} is the optical transmittance of the MRM, ω and ω_0 are the operating and resonant frequencies of the microring in the optical frequency domain, and D is the optical frequency detuning. τ is the total decay time constant of the ring resonator which can be further decomposed according to the equation $1/\tau = 1/\tau_l + 1/\tau_e$, where τ_e is the decay time constant attributed to the ring-to-waveguide coupling and τ_l is the decay time constant attributed to the internal loss of the ring. n_g is the group index of the waveguide and $\partial n/\partial V_j$ is the small-signal index modulation with respect to the junction voltage V_j. According to the mathematical expression in (1), the EO transfer function has one zero and two poles in the s-domain, which introduces the optical peaking effect depending on the frequency detuning D.

Fig. 5 illustrates the EO conversion efficiency as a function of the optical frequency detuning of the Si MRM at a low modulation frequency. The MRM is assumed to operate under the critical coupling condition. In this analysis, we define a normalized frequency detuning $\mathrm{D_n}$, which is the optical frequency detuning divided by half of the 3-dB bandwidth ($1/\tau$) of the microring resonator. The EO conversion efficiency at a low modulation frequency thus can be expressed by

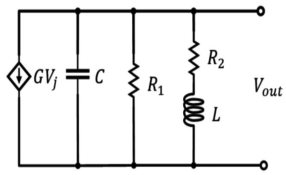

Fig. 7. Equivalent circuit model of EO conversion of the Si MRM.

$$\mathrm{EO}\,(\mathrm{s}\sim 0) = \frac{4}{n_g}\cdot\frac{\partial n}{\partial V_j}\cdot\frac{\omega_0\frac{D}{\tau_e}}{D^2+\frac{1}{\tau^2}}\cdot\frac{\frac{1}{\tau}}{D^2+\frac{1}{\tau^2}} \quad (3)$$

According to (3), the low-frequency EO conversion efficiency is analyzed with respect to different normalized frequency detuning. It is clearly observed that as the $\mathrm{D_n}$ is near 0 (at-resonance) or far from 1 (off-resonance), the EO conversion efficiency decreases. Only when the $\mathrm{D_n}$ equals to $1/\sqrt{3}$, the EO conversion efficiency is maximum.

On the other hand, at higher modulation frequencies, the signal bandwidth can be comparable to the optical bandwidth of the ring resonator. For this case, the dynamics of EO conversion need to be considered, which is corresponding to the rational function at the right-hand side of (1). We analyze the frequency response of EO conversion by varying the normalized frequency detuning of the MRM from 0.4 to 1, which are plotted in Fig. 6. As $\mathrm{D_n}$ is small (0.4), the EO conversion efficiency is generally low at all frequencies. When $\mathrm{D_n}$ is equal to $0.55\sim 1/\sqrt{3}$, the low-frequency EO conversion efficiency is maximum and the 3-dB roll-off frequency is around 55 GHz, which is limited by the optical bandwidth of the ring in this study. As $\mathrm{D_n}$ exceeds 0.55, the optical peaking effect emerges to increase the 3-dB roll-off frequency. The peaking frequency also increases with the normalized frequency detuning. However, despite the increasing roll-off frequency, the EO conversion efficiency at low frequencies drops instead. Attenuated low-frequency EO conversion could cause deformation of the modulated signal.

In fact, the transfer function of EO conversion for the Si microring in (1) is equivalent to the voltage transmittance of an equivalent circuit illustrated in Fig. 7 [18]. According to the circuit configuration, the corresponding transfer function

V_{out}/V_j is then written by

$$EE(s) \equiv \frac{V_{out}}{V_j} = \frac{\mathrm{G}}{\mathrm{C}} \cdot \frac{s + \frac{R_2}{L}}{s^2 + \left(\frac{1}{R_1 C} + \frac{R_2}{L}\right)\mathrm{s} + \frac{1}{LC}\left(\frac{R_2}{R_1} + 1\right)}$$
$$= \mathrm{EO}(\mathrm{s}) \cdot \mathrm{U}_1 \quad (4)$$

where G is the transconductance for the junction voltage V_j converting to the current source in the circuit. V_{out} is the output voltage, and V_{out}/V_j is equivalent to $P_{out}/(P_{in}V_j)$ in value if we assume $\mathrm{U}_1 = 1$ (V) is for unit conversion. By equating (1) with (4), we can find the relationship between the circuit elements and the key ring parameters used in (1), which are given by

$$\mathrm{G} = \frac{2}{n_g} \cdot \frac{\partial n}{\partial V_j} \cdot \frac{\omega_0 \frac{D}{\tau_e}}{D^2 + \frac{1}{\tau^2}} \cdot \frac{1}{R_1} \cdot U_2 \quad (5)$$

$$R_1 = \left[\frac{\tau_e \tau_l}{4}\left(D^2 + \frac{1}{\tau^2}\right) - 1\right] R_2 \quad (6)$$

$$\mathrm{C} = \frac{\tau_e}{2R_1} \quad (7)$$

$$\mathrm{L} = \frac{\tau_l R_2}{2} \quad (8)$$

where U_2= 1 (s•V) for unit conversion. Therefore, varying the frequency detuning D can change the values of all the circuit elements accordingly. This equivalent circuit model can cascade with the circuits in Figs. 2 and 3 to facilitate the analysis of the overall EO conversion efficiency of the Si MRM.

IV. Design of a Silicon Microring Modulator

By combining the equivalent circuit model of EO conversion (Fig. 7) with the circuits illustrated in Figs. 2 and 3, we can accomplish a complete EO conversion model of a Si MRM with respect to a driving voltage applied on the pads. Varying single or multiple circuit elements could significantly influence modulation efficiency and bandwidth, and these elements strongly depend on the device structure and operating condition. In this study, we include an integrated inductor at the metal traces and adjust the optical frequency detuning to engineer the frequency response of a Si MRM. As discussed in the previous section, the inclusion of an inductor in the metal lines can introduce an inductive peaking effect at the first-stage circuit, which further modifies the frequency response of input signal transmission. Meanwhile, detuning the optical frequency of an MRM could also introduce an optical peaking effect. Therefore, the overall frequency response of EO conversion can be tailored by engineering the integrated inductor and the operating wavelength.

To analyze the frequency response of the Si MRM, the total decay time constant of the ring resonator needs to be found first. The Si MRM used in this study operates near the critical coupling condition and has a 3-dB bandwidth of 610 pm (76 GHz), which is corresponding to the decay time constant of 4.2 ps. On the other hand, according to the layered structure of the device and the measured device characteristics (S-parameters), the complete 3-stage equivalent circuit model of the Si MRM can be constructed. We then study the EO conversion efficiency with respect to the normalized frequency detuning $\mathrm{D_n}$ and the inductance of the integrated inductor $\mathrm{L_{ext}}$ at different modulation frequencies. The results are shown in Fig. 8(a) and (b). If the Si MRM is planned to operate at the 50-GHz frequency band (single-tone modulation) with maximum efficiency, the $\mathrm{L_{ext}}$ and $\mathrm{D_n}$ need to be designed around 400 pH and 0.9, respectively. For the 70-GHz frequency band, the optimized inductance and frequency detuning are 200 pH and 1. Therefore, the maximal value of EO conversion efficiency can be accomplished by properly designing the inductance of the integrated inductor and operating the Si MRM at the proper detuning condition.

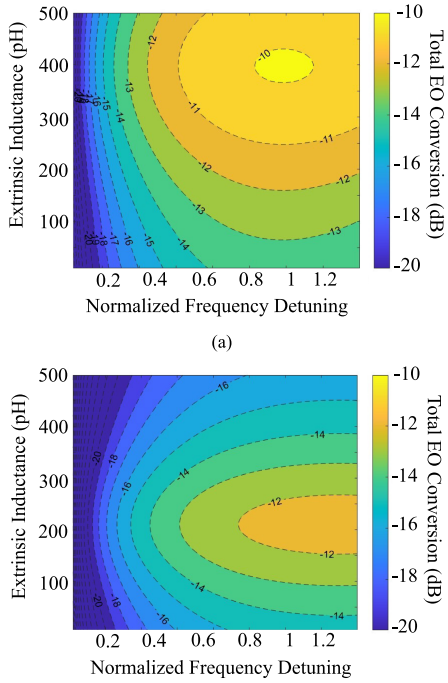

Fig. 8. Color maps of EO conversion efficiency with respect to the inductance and frequency detuning of the Si MRM at the modulation frequencies: (a) 50 GHz and (b) 70 GHz.

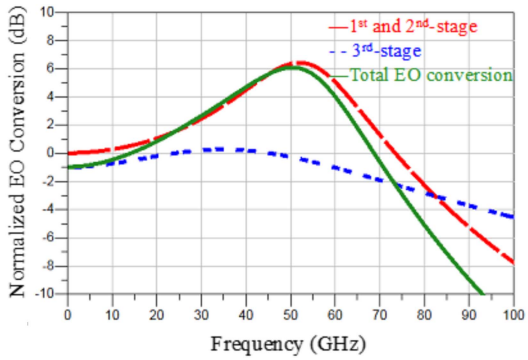

Fig. 9. Frequency response of the Si MRM with an integrated 330-pH inductor, operating at 1 normalized frequency detuning.

Different combinations of the extrinsic inductance and frequency detuning can be used to tailor the spectrum of EO conversion. For example, we consider a Si MRM incorporating a 330-pH inductor and operating it at the condition of 1 normalized frequency detuning. The resulting EO conversion spectrum is shown in Fig. 9, where there is a peak gain occurring at 50 GHz.

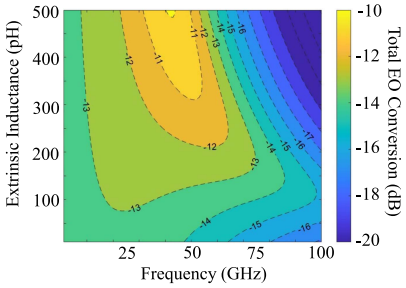

Fig. 10. Color map of EO conversion spectrum with respect to the inductance.

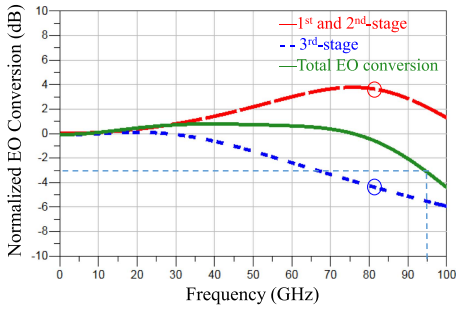

Fig. 11. Frequency response of the Si MRM integrated with a 150-pH inductor.

In fact, this EO conversion can be decomposed into two frequency responses multiplying together; one is the transmission spectrum of the 1st- and 2nd -stage equivalent circuits of the device (red dash curve in Fig. 9) and the other is corresponding to the 3rd -stage equivalent circuit of the microring EO conversion (blue dot curve in Fig. 8). These two frequency responses have the peak gains at 53 GHz and 35 GHz, respectively.

Although the inductive and optical peaking effects can be utilized to enhance the EO conversion efficiency for a specific frequency band, for a broad-band application, we can achieve a flat transmission band with a large 3-dB roll-off frequency. To present this idea, first of all, we choose the normalized frequency detuning to be near $1/\sqrt{3}$ to keep a high EO conversion efficiency at the low modulation frequencies. Next, we analyze the inductance of the integrated inductor and obtain the overall frequency response of the EO conversion, as shown in Fig. 10. In this figure, as the inductance exceeds 300 pH, there exists a significant peak gain on the spectrum. If we choose the inductance to be around 150 pH, a wide and flat EO conversion band is accomplished.

According to the analytic result shown in Fig. 10, we choose the integrated inductor with an inductance of 150 pH and adjust the normalized frequency detuning to be $1/\sqrt{3}$. The simulated frequency response of the Si MRM is displayed in Fig. 11. The original EO conversion spectrum of the MRM without the integrated inductor is represented by the blue dot curve, indicating that the 3-dB bandwidth is around 65 GHz (without optical peaking). By incorporating the 150-pH inductor, the driving voltage has an inductive peaking gain around 80 GHz (red dash curve), which boosts the original bandwidth to 95 GHz (green solid curve) with a flat spectrum. To design a broad-band Si MRM, unlike previous research [16], [23], [24], [25] using optical peaking to extend the 3-dB roll-off frequency, a new design scheme in this study is exploiting the inductive peaking effect and optimizing the optical frequency detuning to achieve a wide and flat modulation band without sacrificing the low-frequency response.

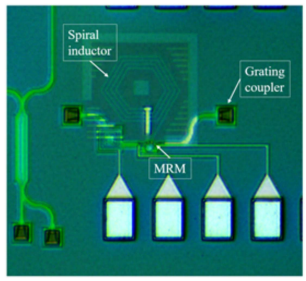

Fig. 12. Fabricated Si MRM integrated with a spiral inductor.

V. Measurement Results

Fig. 12 shows an optical image of the fabricated Si MRM. Two grating couplers are used for coupling light into and out of the Si waveguides coupled to the Si MRM for measurement. 4 electrode pads are deployed to apply RF signals and provide a DC current for tuning the resonant wavelength of the microring resonator. The metal lines are designed with a spiral shape to introduce an extrinsic inductance. The experimental setup to investigate the EO response of the Si MRM is described below. A tunable laser with an optical power of 2.5 dBm is launched into the Si MRM through the grating coupler. This coupling loss is estimated to be 5 dB per end, and the other fiber optics losses from the polarization controller, fibers, and connectors are 0.5 dB. Therefore, the input power prior to the device is estimated to be less than -3dBm so as to prevent nonlinear phase shift due to cavity-enhanced two-photon absorption [26]. Then the RF signal is generated from a 70-GHz vector network analyzer (VNA, Anritsu MS4640B) and passes through a 70-GHz bias tee (Anritsu V251) connected to a DC power supply to provide a reverse bias of 2V. The combined signal is then applied to the pads of the device via a high-frequency G-S probe. The modulated optical signal from the output grating coupler is boosted by an erbium-doped fiber amplifier (EDFA, Thorlabs EDFA100P) and passes through an optical bandpass filter (EXFO XTM-50) to eliminate the unwanted amplified spontaneous emission (ASE) noise. A 70 GHz InGaAs photodetector (Anritsu MN4765B) is used to convert the optical signal back to the RF signal. Finally, the demodulated RF signal is directed to the VNA to analyze the electrical-optical-electrical (E-O-E) S-parameters.

Three devices are examined to verify the design scheme. Two are the Si MRM with integrated inductors of 330 pF and 215 pF, respectively, and the other is the primitive MRM without an inductor. The inductances are extracted according to the measured S11 parameters of the devices and the test structures. The normalized optical frequency detuning is operated near $1/\sqrt{3}$ by tuning the laser wavelength. The measured frequency responses of EO conversion are shown in Fig. 13. The blue curve is the EO response of the MRM with the 330-pH inductor. It has a peaking gain near 50 GHz. The 3-dB bandwidth is about 70 GHz.

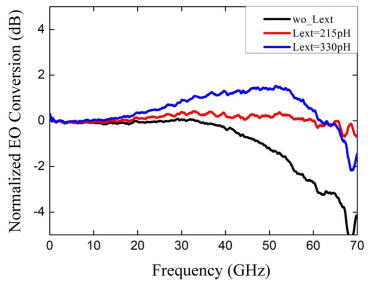

Fig. 13. Measured frequency responses of EO conversion for the Si MRMs with and without inductors.

The red curve is the EO response of the MRM with the 215-pH inductor. Although the 215-pH inductance is different from the optimized value of 150 pH used in Fig. 11, the EO modulation spectrum is still very flat with a wide 3-dB bandwidth over 70 GHz, which is mainly limited by the range of our OVNA measurement system. On the other hand, the measured 3-dB bandwidth of the primitive MRM without an inductor (black curve) is only about 62 GHz. The measured results generally agree well with our analysis in Fig. 10.

VI. Conclusion

In this paper, we study a scheme using both the inductive and optical peaking techniques to tailor the modulation band of a Si MRM. A complete equivalent circuit model of EO conversion is constructed firstly, according to the device structure, material, and operating condition. We incorporate an inductor design at the metal trace of the Si MRM to introduce an additional inductance in the circuit. This inductance can yield an inductive peaking effect to enhance signal transmission at the peaking frequency. Meanwhile, adjusting the operating wavelength or resonant wavelength of the MRM can introduce an optical peaking effect, depending on the optical frequency detuning. Although the previous studies show that optical peaking can extend the 3-dB roll-off frequency of the MRM, the low-frequency response decreases instead. We find the maximal low-frequency response occurs as the optical frequency detuning equals to $1/\sqrt{3}$ of half of the ring's 3-dB bandwidth, provided that the ring operates at the critical coupling condition. Via engineering both the inductance and the optical frequency detuning, the modulation band of the Si MRM can be tailored with more degrees of freedom. We present two types of modulation schemes; one is with a high EO conversion gain at a certain frequency band for microwave photonics, and the other is with a broad, flat EO conversion spectrum for high-speed data transmission. A very high-speed Si MRM with a flat modulation band over 95 GHz (corresponding to a maximum NRZ bitrate of 126 Gbit/s) is expected to be accomplished [28].

References

[1] S. Y. Siew et al., "Review of silicon photonics technology and platform development," *J. Lightw. Technol.*, vol. 39, no. 13, pp. 4374–4389, Jul. 2021.
[2] A. Rahim et al., "Taking silicon photonics modulators to a higher performance level: State-of-the-art and a review of new technologies," *Adv. Photon.*, vol. 3, no. 2, 2021, Art. no. 024003.
[3] C. Li et al., "A 3D-integrated 56 Gb/s NRZ/PAM4 reconfigurable segmented Mach-Zehnder modulator-based Si-photonics transmitter," in *Proc. IEEE BiCMOS Compound Semicond. Integr. Circuits Technol. Symp.*, 2018, pp. 32–35.
[4] D. Petousi et al., "Analysis of optical and electrical tradeoffs of traveling-wave depletion-type Si Mach–Zehnder modulators for high-speed operation," *IEEE J. Sel. Topics Quantum Electron.*, vol. 21, no. 4, Jul./Aug. 2015, Art. no. 3400108.
[5] S. Manipatruni, K. Preston, L. Chen, and M. Lipson, "Ultra-low voltage, ultra-small mode volume silicon microring modulator," *Opt. Exp.*, vol. 18, no. 17, pp. 18235–18242, 2010.
[6] P. Dong et al., "Wavelength-tunable silicon microring modulator," *Opt. Exp.*, vol. 18, no. 11, pp. 10941–10946, 2010.
[7] K. Padmaraju, D. F. Logan, X. Zhu, J. J. Ackert, A. P. Knights, and K. Bergman, "Integrated thermal stabilization of a microring modulator," *Opt. Exp.*, vol. 21, no. 12, pp. 14342–14350, 2013.
[8] W. D. Sacher and J. K. S. Poon, "Dynamics of microring resonator modulators," *Opt. Exp.*, vol. 16, no. 20, pp. 15741–15753, 2008.
[9] J. Fujikata et al., "High-speed Ge/Si electro-absorption optical modulator in C-band operation wavelengths," *Opt. Exp.*, vol. 28, no. 22, pp. 33123–33134, 2020.
[10] K. Van Gasse, J. Verbist, H. Li, G. Torfs, J. Bauwelinck, and G. Roelkens, "Silicon photonics radio-over-fiber transmitter using GeSi EAMs for frequency up-conversion," *IEEE Photon. Technol. Lett.*, vol. 31, no. 2, pp. 181–184, Jan. 2019.
[11] W. Shen, G. Zhou, J. Du, L. Zhou, K. Xu, and Z. He, "High-speed silicon microring modulator at the 2 μm waveband with analysis and observation of optical bistability," *Photon. Res.*, vol. 10, no. 3, pp. A35–A42, 2022.
[12] Z. Yong et al., "U-shaped PN junctions for efficient silicon Mach-Zehnder and microring modulators in the O-band," *Opt. Exp.*, vol. 25, no. 7, pp. 8425–8439, 2017.
[13] D. G. Rabus and C. Sada, "Ring resonators: Theory and modeling," in *Integrated Ring Resonators*. Berlin, Germany: Springer, 2020, pp. 3–46.
[14] J. Müller et al., "Optical peaking enhancement in high-speed ring modulators," *Sci. Rep.*, vol. 4, no. 1, pp. 1–9, 2014.
[15] Y. Ehrlichman, A. Khilo, and M. A. Popović, "Optimal design of a microring cavity optical modulator for efficient RF-to-optical conversion," *Opt. Exp.*, vol. 26, no. 3, pp. 2462–2477, 2018.
[16] H. Li et al., "A 112 Gb/s PAM4 silicon photonics transmitter with microring modulator and CMOS driver," *J. Lightw. Technol.*, vol. 38, no. 1, pp. 131–138, Jan. 2020.
[17] M. Shin et al., "A linear equivalent circuit model for depletion-type silicon microring modulators," *IEEE Trans. Electron. Devices*, vol. 64, no. 3, pp. 1140–1145, Mar. 2017.
[18] S. Karimelahi, W. Rahman, M. Parvizi, N. Ben-Hamida, and A. Sheikholeslami, "Optical and electrical trade-offs of rib-to-contact distance in depletion-type ring modulators," *Opt. Exp.*, vol. 25, no. 17, pp. 20202–20215, 2017.
[19] B. Pile and G. Taylor, "Small-signal analysis of microring resonator modulators," *Opt. Exp.*, vol. 22, no. 12, pp. 14913–14928, 2014.
[20] Y. Ban, J. M. Lee, B. M. Yu, S. H. Cho, and W. Y. Choi, "Small-signal frequency responses for Si micro-ring modulators," in *Proc. Opt. Interconnects Conf.*, 2014, pp. 47–48.
[21] M. Kim et al., "A large-signal equivalent circuit for depletion-type silicon ring modulators," in *Proc. Opt. Fiber Commun. Conf.*, 2018, pp. 1–3.
[22] Y. Kim et al., "Parametric optimization of depletion-type Si micro-ring modulator performances," *Japanese J. Appl. Phys.*, vol. 58, no. 6, 2019, Art. no. 062006.
[23] Y. Zhang et al., "200 Gbit/s optical PAM4 modulation based on silicon microring modulator," in *Proc. Eur. Conf. Opt. Commun.*, 2020, pp. 1–4.
[24] J. Sun, R. Kumar, M. Sakib, J. B. Driscoll, H. Jayatilleka, and H. Rong, "A 128 Gb/s PAM4 silicon microring modulator with integrated thermo-optic resonance tuning," *J. Lightw. Technol.*, vol. 37, no. 1, pp. 110–115, Jan. 2019.
[25] H. Wang, T. Horikiri, and T. Kobayashi, "Polarization-entangled mode-locked photons from cavity-enhanced spontaneous parametric down-conversion," *Phys. Rev. A*, vol. 70, no. 4, 2004, Art. no. 043804.
[26] B. Abiri et al., "Bandwidth enhancement technique using inductive peaking," U.S. Patent 9,651,803 B2, May 2017.
[27] H. Kao, M. Lin, and M. C. Lee, "Optimized design of inductive-peaking Si microring modulator for operating bandwidth over 65 GHz," in *Proc. Conf. Lasers Electro-Opt. Pacific Rim*, 2022, Paper CTuA11D_02.
[28] M. Forghani and B. Razavi, "Circuit bandwidth requirements for NRZ and PAM4 signals," in *Proc. IEEE Int. Symp. Circuits Syst.*, 2022, pp. 990–994.